REVIEW ARTICLE | SEPTEMBER 01 2016

Novel silicon phases and nanostructures for solar energy conversion

Stefan Wippermann; Yuping He; Márton Vörös; Giulia Galli

Appl. Phys. Rev. 3, 040807 (2016)
https://doi.org/10.1063/1.4961724
CHORUS

APPLIED PHYSICS REVIEWS

Novel silicon phases and nanostructures for solar energy conversion

Stefan Wippermann,[1] Yuping He,[2] Márton Vörös,[3] and Giulia Galli[3]
[1]*Interface Chemistry and Surface Engineering Department, Max-Planck-Institut für Eisenforschung GmbH, Max-Planck-Straße 1, 40237 Düsseldorf, Germany*
[2]*Sandia National Laboratories, Livermore, California 94551-0969, USA*
[3]*Institute for Molecular Engineering, University of Chicago, Chicago, Illinois 60637, USA and Argonne National Laboratory, Lemont, Illinois 60439, USA*

(Received 8 April 2016; accepted 27 July 2016; published online 1 September 2016)

Silicon exhibits a large variety of different bulk phases, allotropes, and composite structures, such as, e.g., clathrates or nanostructures, at both higher and lower densities compared with diamond-like Si-I. New Si structures continue to be discovered. These novel forms of Si offer exciting prospects to create Si based materials, which are non-toxic and earth-abundant, with properties tailored precisely towards specific applications. We illustrate how such novel Si based materials either in the bulk or as nanostructures may be used to significantly improve the efficiency of solar energy conversion devices. [http://dx.doi.org/10.1063/1.4961724]

TABLE OF CONTENTS

I. INTRODUCTION

Silicon, the second most earth abundant element, is widely used for electronic applications, integrated circuits, and photovoltaics. The thermodynamic ground state of Si has a diamond structure (Si-I), it has been extensively studied both theoretically and experimentally, and its properties are well understood. Diamond Si has an indirect band gap, preventing its use in many optoelectronic applications, such as, e.g., light emitting diodes and thin film photovoltaics, which require efficient absorption properties. It is thus highly desirable to explore possible novel forms of Si with improved light absorption and electronic properties tuned specifically towards solar energy conversion applications.

The phase diagram of Si exhibits a multitude of both low and high density polymorphs, many of which are metastable at ambient conditions (cf. Fig. 1). Under pressure, bulk Si retains its cubic diamond (cd, Si-I) structure up to ∼11.7 GPa.[1] At higher pressure, Si-I transforms into the metallic β-tin phase (Si-II), whose stability interval is rather small. On further pressure increase beyond ∼15 GPa, the β-tin phase transforms first into an orthorhombic *Imma* phase, and then into a simple hexagonal one (sh, Si-V). Above 42 GPa, a hexagonal close packed (hcp) solid has been observed, with the orthorhombic *Cmca* phase (Si-VI) formed as an intermediate within 40–42 GPa. At 78 GPa, a face centered cubic (fcc) solid is obtained which remains stable up the highest presently investigated pressure of ∼250 GPa.

All the phases above 12 GPa are metals. The semiconductor-metal transition from the covalently bonded diamond to metallic high pressure phases is irreversible, due to a significant kinetic barrier. Releasing pressure does not lead to recovering the Si-I phase but instead to a series of metastable high-density solids with distorted tetrahedral bonding.

Under slow pressure release starting from β-tin, the rhombohedral R8 phase (Si-XII) is obtained at ∼8 GPa, followed by a transition to BC8 (Si-III) at ∼2 GPa. Si-III remains metastable at ambient conditions. Subsequent thermal annealing at moderate temperature leads to the formation of hexagonal diamond (hd, Si-IV). If β-tin is decompressed rapidly within less than ∼100 ms, two additional phases may be observed, Si-VIII and Si-IX, which are believed to consist of large tetragonal unit cells. However, to date, only incomplete structural information is available. It has been proposed that Si-IX has the *Ibam* structure.[2] A recent study suggested also the $P4_2/m$ and P-4 structures as possible candidates for Si-IX.[3] Indentation experiments suggested the existence of a previously unobserved Si-XIII phase, the structural details of which are largely unknown.[4] Two further Si polymorphs were predicted theoretically, ST12 (Ref. 5) and a body centered tetragonal (bct) phase,[6] the latter was not yet observed experimentally.

To add to the complexity of the behavior of Si observed upon decompression, a temperature-dependent study reported the formation of the cubic diamond phase at high temperatures (∼400–500 K), whereas low temperature decompression (∼100 K) yielded amorphous Si. A recent study employed ultrashort laser pulses to locally induce pressures and temperatures significantly higher than those attained in diamond anvil cell or

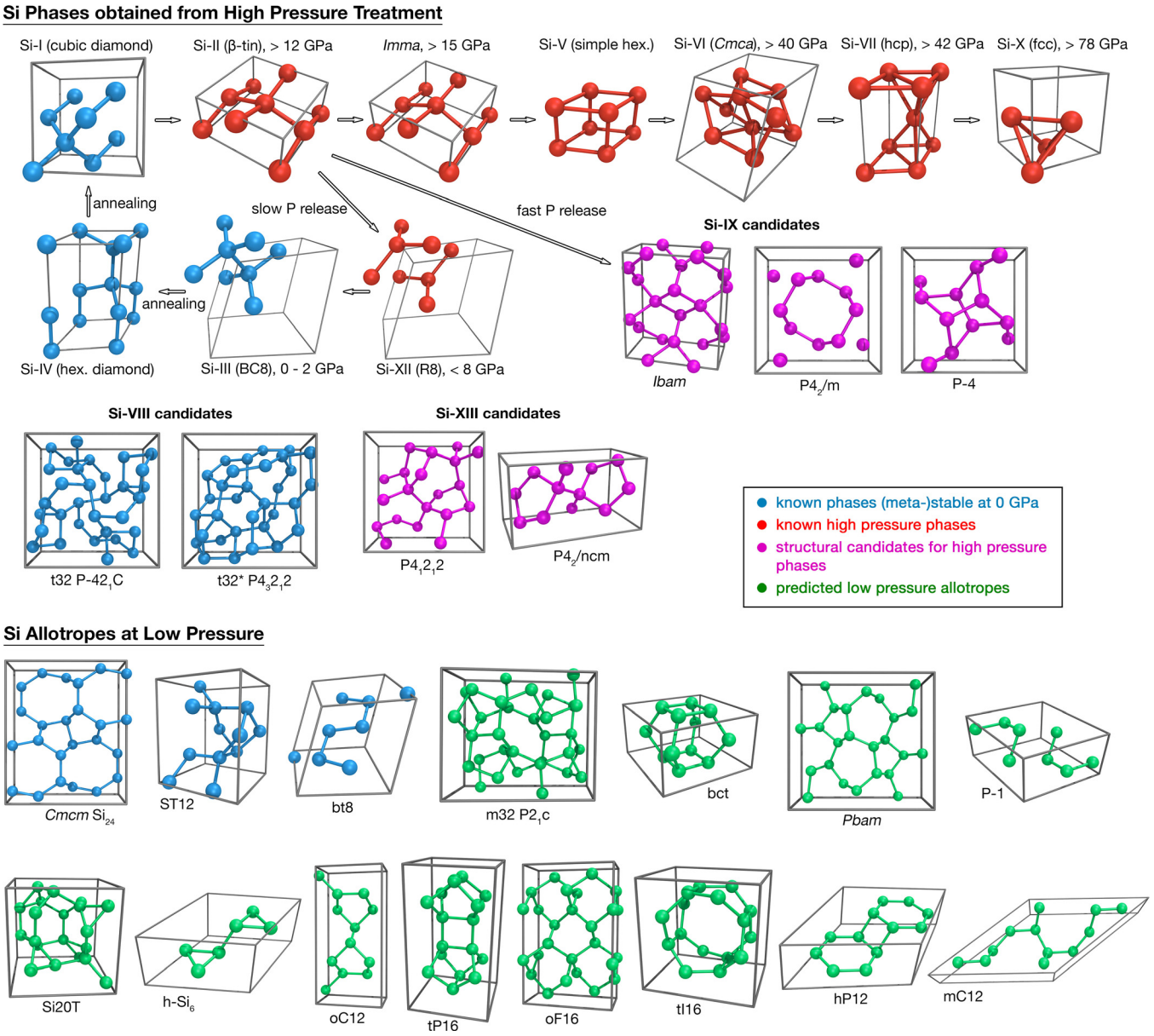

FIG. 1. Schematic overview of silicon high pressure phases (red) and low pressure low energy allotropes that can potentially be stabilized at ambient conditions. Structures known to exist at ambient conditions are marked in blue. Theoretically proposed but not yet observed structures are shown in green. Violet denotes structures proposed for the still elusive Si-IX and Si-XIII phases. See text for details.

indenter experiments,[7] thus permitting, upon cooling, the freezing of local regions of Si into phases that are otherwise inaccessible due to kinetic barriers. These experiments allowed for the experimental observation of ST12, and the existence of bt8 was reported for the first time, as well as that of two additional tetragonal and two monoclinic phases. All phases remained metastable at ambient conditions. This is of particular interest because the unknown Si-VIII and Si-IX structures are believed to be tetragonal with equally large unit cells. Femtosecond laser pulse induced shock waves in Si were also reported to lead to the formation of BC8 and R8 (Ref. 8) phases.

Bulk BC8 is a semi metal and thus not directly usable for solar energy conversion devices. However, R8 and hexagonal diamond (Si-IV) have been considered as possible light absorbers for solar energy conversion. Biaxial tensile strain in excess of 4% leads to an indirect to direct band gap transition (from the Si-IV indirect gap of 0.95 eV into a direct gap of 0.7–0.9 eV (Ref. 9)). R8 on the other hand exhibits a much smaller direct gap (∼1.2 eV) compared with Si-I (∼3.4 eV), even if unstrained, and a significantly improved overlap of the optical absorption with the solar spectrum.[10] The indirect gap of R8 (∼0.24 eV), however, is rather small.

Recently, two new Si structures have been proposed theoretically, P-1 (Ref. 11) and Si20T,[12] both of which have quasi-direct gaps of ≃1.5 eV. In addition, another six dynamically stable allotropes with either direct or quasidirect gaps (oC12, tP16, oF16, tI16, hP12, and mC12) have been proposed from *ab initio* calculations.[13] Recent *ab initio* random structure searches identified solids with $P4_2/ncm$[14] and $P4_12_12$ (Ref. 15) symmetries as possible candidates for the elusive Si-XIII phase, and a new low energy structure (*Pbam*) with an estimated direct gap of 1.4 eV.[15] Another recent study identified a dynamically and thermally stable hexagonal phase, named h-Si_6, with a direct band gap of 0.61 eV.[16] Following

the initial steps taken by Ref. 17 in using global optimization methods to search for structures with desired optoelectronic properties, the authors of Ref. 18 computationally designed a dipole-allowed direct band gap Si-based superlattice.[18]

Similar to the high density Si allotropes, low density Si clathrates, i.e., type-I (Si_{46}), type-II (Si_{136} and Si_{34}), type-III, type-VIII, and type-IX,[19] have rich morphologies. Clathrates are cage structures formed by host atoms (i.e., group IV) enclosing guest atoms (i.e., group I and II). It has been suggested that they behave as a phonon-glass and an electron-crystal,[20] and they have been extensively studied for thermoelectric applications. Recently, Si based clathrates have drawn attention for photovoltaic applications as a result of their tunable quasi-direct band gap in the range needed for optimal performance according to the Shockley-Queisser (SQ) limit.[21–24] Si-based clathrates without guest atoms in the cages are neutral, and thus they are intrinsic semiconductors. The guest-free low density phases are metastable at ambient conditions. Interestingly, a recent study showed that type-II clathrate Si_{34} undergoes a phase transformation to the β-tin phase at the same pressure (11.5 GPa) as diamond Si.[25] In order to maintain their stability at ambient conditions, electropositive guest species are generally required. However, when such guest atoms occupy the cages, they donate electrons to the framework making the material metallic and thus not useful for photovoltaic applications. Recently, Kim *et al.*[26] reported the synthesis of a new *Cmcm* Si_{24} allotrope free of metals, with open channels along the *a*-axis, formed from six and eight membered sp^3 silicon rings, and with a quasi-direct band gap of 1.3 eV. Baranowski and coauthors[24] successfully synthesized a type-II Si-Ge clathrate alloy. By changing the Ge content, they could tune the band gap in the range of 0.8–1.8 eV. An alternative method to make Si clathrates semiconducting is to compensate the charge of the guest atom by doping the framework with an acceptor. Recently, a type-I clathrate $K_8Al_8Si_{38}$ was synthesized, and by using *ab initio* calculations and spectroscopic and Hall mobility measurement, it was shown to be a promising material for photovoltaic applications.[27] It has a quasi-direct band gap of ~1.0 eV. This band gap is smaller than the optimal one (1.4 eV) and it might be improved at the nanoscale.[28]

Although only certain types of clathrates were discovered in experiments, Amsler *et al.*[23] recently conducted a computational search and explored 44 metastable low density silicon clathrates with potential use in photovoltaic applications. Solutions to the Kelvin problem, how to partition three-dimensional space into cells of equal volume with minimal area, led to the discovery of another series of new low density Si allotropes that are structurally related to clathrates.[29]

II. NANOSTRUCTURED SILICON

In the following, we discuss three classes of nanostructured silicon: (i) Clathrates, which exhibit a wide range of quasi-direct band gaps and carrier concentrations, depending on host and guest atom types. They can be synthesized as nanostructured bulk materials by simple mixing and baking approaches. (ii) Embedded Si nanoparticles (NPs), enabling the use of multi-exciton generation (MEG) processes to increase photocurrents, together with tunable band gaps and efficient photoluminescence. (iii) Si NPs with high pressure core structures, which simultaneously yield efficient MEG and band gaps suitably small for MEG-based solar energy conversion.

A. Clathrates

Here, we focus on $K_8Al_8Si_{38}$, a clathrate that was proposed as a promising photovoltaic material. It was studied with *ab initio* calculations, which showed that the system has a quasidirect band gap of ~1.0 eV, in agreement with the optical measurements (1.3 eV). The gap is tunable by strain engineering within the IR and visible ranges. In addition, excited electrons and holes generated upon absorption were shown to be spatially separated on different cages, a favorable configuration to avoid recombination, and carrier mobilities were found to be superior to those of *a*-Si.

Six snapshots of the $K_8Al_8Si_{38}$ structure were generated computationally, using the guidelines for site occupancy proposed by Christensen *et al.*[30] We then computed the total energies of the six samples using *first principles* density functional theory (DFT) calculations within the Perdew-Burke-Ernzerhof (PBE) approximation,[31,32] and we identified the two most stable configurations. These turned out to be consistent with those recently observed experimentally in the type-I clathrate $Ba_8Al_xSi_{46-x}$ (see Ref. 33) and, most importantly, with those found in the single crystal $K_8Al_8Si_{38}$ grown in the experiments of Ref. 27.

Having identified the most stable sets of configurations of $K_8Al_8Si_{38}$, we computed the band structures (Fig. 2) of several of those, with Al substituted at different sites, in order to mimic the range of atomic substitutions possibly existing in the real material. Most calculations were conducted at the DFT level and one sample (A) was carefully analyzed using many body perturbation theory (MBPT) at

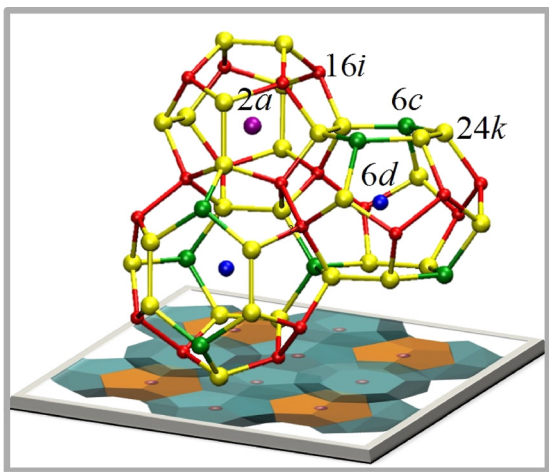

FIG. 2. Ball and stick representation of the type-I clathrate investigated in this work: $K_8Al_8Si_{38}$, composed of dodecahedral and tetrakaidecahedral cages. Within the Wyckoff sites representation of the structure, the centers of the cages are denoted by 2a (purple) and 6d (blue) for dodecahedral and tetrakaidecahedral cages, respectively; the host structure is represented by three inequivalent crystallographic sites: 6c (green), 16i (red), and 24k (yellow). Reproduced with permission from He *et al.*, Energy Environ. Sci. **7**, 2598 (2014). Copyright 2014 Royal Society of Chemistry.

the G_0W_0 level.[34] The position of Al significantly influences the position of the valence bands, while the conduction bands (CBs) are largely unaffected (see Figs. 3(a) and 3(b)). Fig. 3(c) shows the G_0W_0 corrected band structure of sample A with respect to that obtained at the DFT-PBE level. We found a rigid shift of the uppermost valence band (VB) to lower energy (0.04 eV) and of the lowest conduction band (CB) to higher energy (0.21 eV), yielding a band gap (0.81 eV) increase of approximately 45% with respect to that computed within DFT-PBE (0.56 eV). We then assumed that a similar increase would approximately apply to all other samples, in going from the DFT-PBE to the G_0W_0 levels of theory (all samples have similar geometries and exhibit the same kind of bonds). The computed gaps vary between 0.44 and 0.79 eV within PBE and between 0.64 and 1.15 eV within G_0W_0 under normal conditions. Irrespective of the sample and the level of theory, we found that all models have direct or quasi-direct band gaps, with differences between direct and indirect ones of at most ∼0.14 eV.

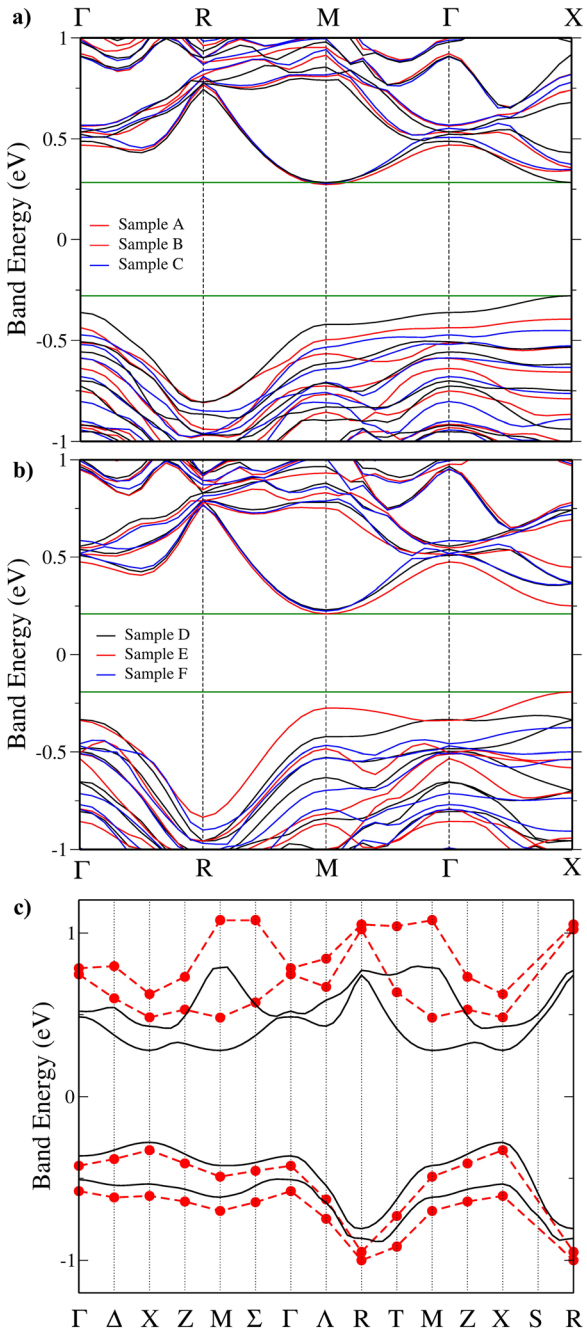

FIG. 3. (a) Band structure of $K_8Al_8Si_{38}$ with Al on five 6c sites, two 24k sites, and one 16i site (5c2k1i configurations), for samples A (black), B (red), and C (blue), calculated using DFT-PBE. (b) Band structure of $K_8Al_8Si_{38}$ with Al on six 6c sites, two 16i sites (6c2i configurations) for samples D (black), E (red), and F (blue), calculated using DFT. (c) Band structure of $K_8Al_8Si_{38}$ (sample A) calculated using DFT-PBE (black) and many body perturbation theory within the G_0W_0 approximation (red), respectively. Reproduced with permission from He *et al.*, Energy Environ. Sci. **7**, 2598 (2014). Copyright 2014 Royal Society of Chemistry.

The direct and indirect band gaps were also estimated experimentally in Ref. 27. Measuring the absorbance, converting it to the Kubelka-Munk function F(R), and using a Tauc plot a direct band gap of 1.29 eV and an indirect band gap of 1.06 eV were obtained, in excellent agreement with the theoretically predicted values of ∼1.0 eV.

We also analyzed the variation of the gaps caused by possible strain fields present in the material due to, e.g., growth conditions. We found a decrease (increase) of about 23% in the gap under 2% compression (tensile strain), with no notable change in the shape of the bands and hence no modification of the nature of the gaps that remained (quasi)-direct. Hence, we concluded that the computed band gap within G_0W_0 under the effect of strain is between 0.5 and 1.4 eV. These results suggest that one may tune the optical absorption of the material in a range between IR and visible by strain engineering, with great advantage with respect to materials that absorb just in a narrow energy window.

In addition to efficient absorption, key properties of materials for photovoltaic applications are the spatial localization of electrons and holes and their mobilities. Fig. 4 shows the calculated square moduli of the valence band maximum (VBM, red) and conduction band minimum. (CBM, blue) wave functions of sample A. Interestingly, we found

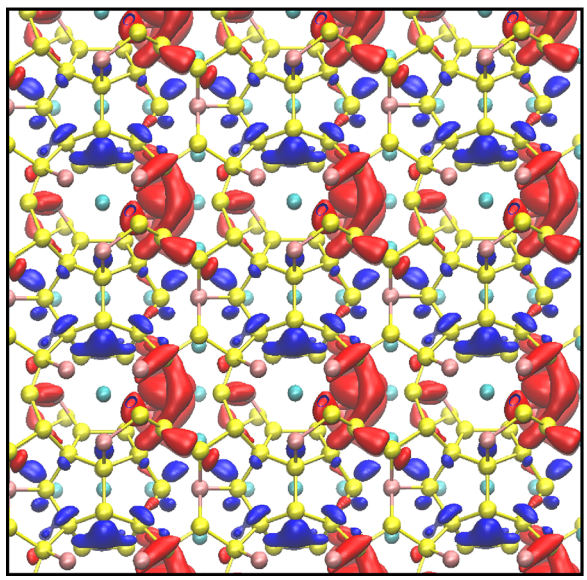

FIG. 4. Isosurfaces of the square moduli of the valence band maximum (red) and conduction band minimum (blue) single particle states of the type-I clathrate $K_8Al_8Si_38$; yellow, pink, and cyan spheres represent Si, Al, and K atoms, respectively. Reproduced with permission from He *et al.*, Energy Environ. Sci. **7**, 2598 (2014). Copyright 2014 Royal Society of Chemistry.

that the VBM is localized in the large cages around the Al atoms, while the CBM is localized on the small cages around the Si atoms, with very limited spatial overlap between the two, indicating a low probability of charge recombination.

To estimate the carrier mobilities of electrons and holes as a function of concentration and temperature (T), a single band Kane model[35] was employed, where all the parameters were derived from *first principles*.[27] We found that the electron and hole mobilities of the type-I clathrate $K_8Al_8Si_{38}$, as shown in Fig. 5, are smaller than those of diamond Si[36–38] by a factor of 6–10 at room temperature. The lower values of the mobilities are partly due to the small amount of disorder present in the cages. However, the computed values of the mobility μ are better than those of SnS[39] and comparable to those of Cu_2O,[40] which are promising semiconductors for photovoltaic applications. Importantly, we found that the μ of $K_8Al_8Si_{38}$ is much superior to those of, e.g., *a*-Si: $1\,cm^2\,V^{-1}\,s^{-1}$ for electrons and $0.01\,cm^2\,V^{-1}\,s^{-1}$ for holes[41–44] and to those of organic materials: $\sim 0.008\,cm^2\,V^{-1}\,s^{-1}$ for electrons and ~0.002 for holes.[45] In addition, the ratio μ_e/μ_h is ~5 in $K_8Al_8Si_{38}$, while it can be as high as 100 in *a*-Si (it is ~3 in c-Si).

B. Embedded Si nanoparticles

Another approach actively explored to create Si materials with tailored properties is based on embedded Si nanostructures, such as, e.g., superlattices of Si nanoparticles inside a host matrix.[46,47] As pointed out in the Introduction, BC8 (Si-III) is one of the Si polymorphs that is known to remain metastable at ambient pressure. In its bulk form, however, DFT-local density approximation (LDA) calculations found it to be a semimetal with a direct band overlap of 0.8 eV at the H point in the bcc Brillouin zone.[48] While measurements on BC8 confirmed this classification, the nature of the band overlap was suggested to be indirect with a value of 0.3 eV.[49] Quasiparticle calculations in the G_0W_0 approximation estimated a reduction of the overlap obtained in LDA by ~0.33 eV.[50] BC8 therefore is a particularly interesting candidate for exploiting quantum confinement effects to obtain Si structures with adjustable gaps, as a function of size, possibly in a wide energy range.

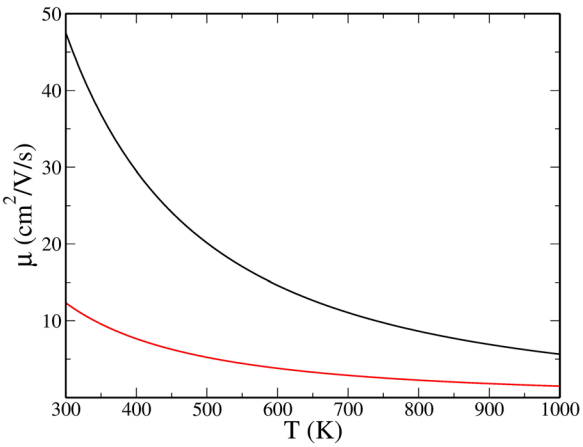

FIG. 5. Calculated carrier mobilities (electrons: black curve and holes: red curves) of type-I clathrate $K_8Al_8Si_{38}$ as a function of temperature (T) with a carrier concentration of 1×10^{18} cm^3, using the single Kane band model (see the text). Reproduced with permission from He *et al.*, Energy Environ. Sci. **7**, 2598 (2014). Copyright 2014 Royal Society of Chemistry.

One of the advantages of nanoparticles is the possibility to exploit efficient multi-exciton generation (MEG) processes, where one incoming photon creates multiple electron-hole pairs. In 2002, Nozik suggested that in nanoparticles (NPs) the effective Coulomb interaction is enhanced by quantum confinement and the electronic screening decreased, driving the efficiency of MEG to promisingly high values.[51] In 2004–2006, the Klimov group demonstrated that efficient MEG may indeed be obtained in semiconducting NPs (see, e.g., Ref. 52), triggering intense theoretical and experimental interest.[53–61] While the efficiency enhancement reported in Ref. 52 was later questioned,[53] the presence of MEG was eventually verified in colloidal NPs, albeit with a reduced magnitude.[56] In 2012, Semonin *et al.*, followed by Zhai *et al.* shortly afterwards, demonstrated that the excess electrons generated by MEG can be efficiently extracted from the NPs and transferred to the electrodes of PbSe and $PbS_{0.9}Se_{0.1}$ NP solar cells; the MEG enhanced the external quantum efficiency above 100% within a region of the solar spectrum.[62,63]

The remaining challenges for harvesting MEGs in nanoparticles include the high energy activation threshold, estimated theoretically to be twice the optical gap but found experimentally around thrice the gap. Therefore, the solar photons can be best captured by multi-exciton generation in materials with gaps in the 0.5–1.0 eV range.[64] Moreover, for concentrated solar cells with a concentration factor of 500, the optimal gap has been shown to be as low as 0.1 eV.[65]

At the nanoscale, quantum confinement enhances the Coulomb interaction, thereby allowing for efficient MEG,[51] but it also leads to an increase of the gap and a reduction of the density of states (DOS) at any given energy. The increase of the gap with decreasing NP radius can swiftly shift the MEG threshold energy outside the solar spectrum. On the other hand, lowering the gap may reduce the effective Coulomb interaction and thus MEG efficiency. Therefore, two competing requirements have to be satisfied by identifying semiconducting NPs exhibiting simultaneously (i) a small excitation gap and a DOS only moderately reduced with respect to the bulk and (ii) efficient MEG despite suitably small gaps.

Luo *et al.* systematically investigated a range of semiconductor materials suitable to harvest MEG.[54] They showed that Si nanoparticles in the diamond structure may exhibit highly efficient MEG, but their band gap unfortunately is too large, i.e., it does not meet the requirements imposed by the solar spectrum. In a recent paper, we proposed that nanoparticles with core structures made from Si polymorphs, in particular, BC8, offer a way to tune the electronic gap toward suitable values while retaining efficient MEG.[66]

In 2006, Arguirov *et al.* reported the formation of BC8 Si NPs within amorphous Si in *a*-Si/SiO_2 multilayer stacks.[69] In addition, Smith *et al.*[8] showed that R8 and BC8 NPs are formed when "black silicon" is produced by irradiating highly doped Si surfaces with femtosecond laser pulses. The authors argued that pressure waves generated by the fs-pulses first amorphized regions of the sample and then

induced the nucleation of R8 and BC8 NPs within these regions. Formation of nanocrystalline BC8 regions was also observed in nano-grinding experiments,[70] in SiGe epilayers,[71] and in nanoindentation experiments.[72–75] Recently, even direct colloidal synthesis of BC8 nanoparticles was reported, which would completely bypass the need for high pressure synthesis.[76]

These experiments suggest that Si NPs with core structures based on high pressure Si phases are promising candidates to exhibit a lower gap than Si-I NPs and low energy optical absorption, especially the BC8 phase, which is gapless in the bulk. However, a detailed analysis is required to establish whether the strength of the Coulomb interaction is preserved and whether efficient MEG is still present in such Si NPs.

C. High pressure core structures

To explore the possible advantages of Si NPs with high pressure core structures, we carried out electronic structure calculations within DFT and MBPT. We used the local density approximation (LDA)[77] and norm-conserving pseudopotentials[78] with an energy cutoff of 35 Ry, and the Quantum Espresso package.[79] Quasiparticle energies within the G_0W_0 scheme[80] were obtained by employing the approach of Nguyen *et al.*, which avoids the explicit calculation of empty electronic states and the inversion of large dielectric matrices.[81] Based on the results of our previous study[82] and the findings of Refs. 83 and 84, we assumed that the major contribution to MEG comes from impact ionization (II) processes and we approximated MEG rates with II rates. We used the Fermi Golden Rule to obtain the decay rate of excitons to bi-excitons. The initial exciton and final bi-exciton states were approximated as singly and doubly excited Slater-determinants, built up from DFT orbitals[82] in the PBE generalized gradient approximation.[31] To account for the dielectric screening within our G_0W_0 and II calculations, we computed the dielectric matrix within the random phase approximation (RPA) using iterative techniques.[85]

The core geometry of the Si NPs was built by isolating a sphere of a given radius from the structure of the respective Si bulk phases. The radius and center of this sphere were chosen so as to obtain NPs with no more than two dangling bonds per surface atom. All dangling bonds were saturated with hydrogen atoms. The whole structure was then allowed to relax to the nearest local energy minimum. Fig. 6 shows the resulting final geometries of Si NPs for a diameter of ∼1 nm.

The electronic gap of NPs with various core structures as a function of size is shown in Fig. 7 and Table I. Sizes are given as twice the average radial distance of the NP surface atoms to the center, with size error bars representing the corresponding standard deviation. The BC8 NPs have significantly smaller gaps than all the other nanoparticles. For example, at the LDA level, the gap of a BC8 NP of diameter 2.5 nm is 1 eV lower than that of Si-I NPs of the same size. This substantial difference is consistent with the fact that BC8 is a semi-metal in the bulk. Our result is also in agreement with earlier empirical tight binding calculations.[86]

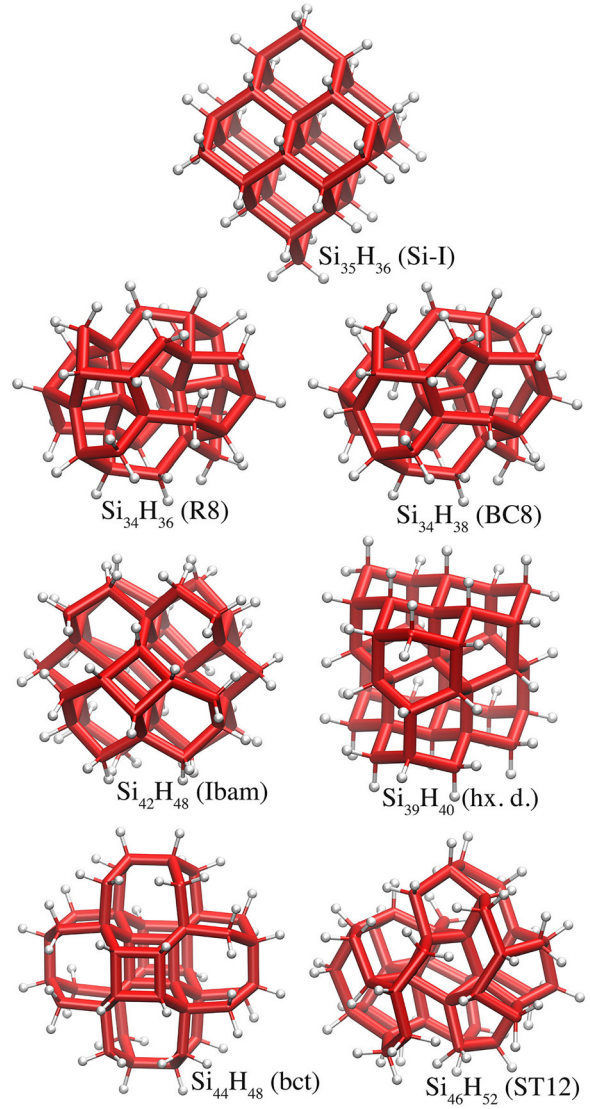

FIG. 6. Structural models of ∼1 nm hydrogenated Si NPs with Si-I, Si-IV (hexagonal diamond), Si-XII (R8), Si-III (BC8), *Ibam*, bct, and ST-12 core structures. Reproduced with permission from Wippermann *et al.*, Phys. Rev. Lett. **110**, 046804 (2013). Copyright 2013 American Physical Society.

Given the tendency of local DFT calculations to underestimate band gaps, we performed quasiparticle calculations in the G_0W_0 approximation for NP diameters up to 1.5 nm (∼144 Si atoms), to assess the validity of the trends observed within LDA. As expected, all computed G_0W_0 gaps are larger than the LDA ones; however, the same trends as a function of the NP diameter were found at both levels of theory (see Table I).

Both LDA and G_0W_0 energy gaps for larger nanoparticles were estimated by fitting the calculated NP and bulk gaps by a power law. The fits are reported in Table I and Fig. 7. At 2.5 (8.0) nm, the Si-I G_0W_0 gaps are 3.6 (2.2) eV and those of BC8 are 2.1 (0.7) eV. We emphasize that at the experimentally accessible diameter of 4 nm to 8 nm, the G_0W_0 gap of BC8 NPs is 1.4 eV to 0.7 eV, near optimal for solar applications.

The quasi particle gaps obtained here are an upper bound to optical gaps, as excitonic effects are not taken into account[87–89] and they may expected to be larger than in the

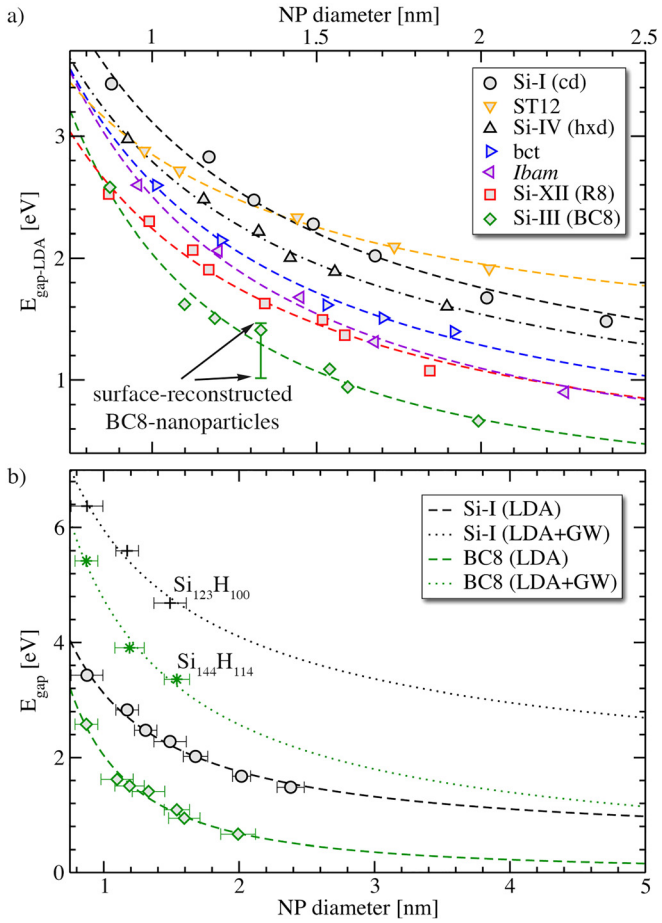

FIG. 7. Electronic gaps of hydrogenated Si nanocrystals as a function of the nanoparticle (NP) diameter computed using (a) the Local Density Approximation (LDA) and (b) many body perturbation theory within the G_0W_0 approximation (G_0W_0). Symbols and lines refer to calculated values and fits (cf. Table I), respectively. Sizes are given as twice the average radial distance of the NP surface atoms to the NP center, with size error bars representing the standard deviation. The core structures of the NPs are labeled in the inset according to the nomenclature used for tetrahedrally bonded bulk Si phases (see text). Reproduced with permission from Wippermann *et al.*, Phys. Rev. Lett. **110**, 046804 (2013). Copyright 2013 American Physical Society.

TABLE I. Electronic gaps of nanoparticles ($E_{g,NP}$) and bulk phases (E_g) obtained using the G_0W_0 approximation. G_0W_0 bulk gaps are taken from Refs. 50, 67, and 68. $E_{g,NP}$ were computed for particles up to ~1.5 nm in G_0W_0 (see Fig. 7) and extrapolated to 4 nm and 8 nm using the relation $E_{g,NP} = E_{g,bulk} + a \cdot ([\text{nm}]/d)^b$, where d is the NP diameter and a, b are fitting constants. The high pressure Si phases (left column) are defined in the text. Reproduced with permission from Wippermann *et al.*, Phys. Rev. Lett. **110**, 046804 (2013). Copyright 2013 American Physical Society.

	$E_{g,NP}$ (eV) (G_0W_0)					*Fitting constants*		
Phase	0.9 nm	1.2 nm	1.5 nm	4 nm	8 nm	Eg (eV)	*a* (eV)	*b*
cd	6.37	5.60	4.69	2.95	2.24	*1.12*	*4.84*	*0.70*
BC8	5.42	3.91	3.35	1.37	0.74	*0.00*	*4.75*	*0.88*
hd	5.89	5.16				*0.95*		
Ibam	5.24	4.51						
R8	4.96	4.37				*0.24*		
bct	5.35	4.94						
ST12	5.57	5.30				*1.54*		

bulk, as suggested by quantum Monte Carlo (QMC) calculations.[90] In addition, several other factors contribute to lowering the quasi particle gaps, including surface reconstruction (cf. Fig. 8),[82,91] symmetry breaking, ligand, pressure effects, and geometrical distortions at finite temperature. Many of these possibilities have already been explored in the past in the case of Si-I NPs.[90,92–99] To estimate the magnitude of these effects, we calculated the gaps of surface reconstructed 1.35 nm BC8 NPs for all possible permutations of surface bonds, generated by rearranging the available twofold coordinated surface Si-atoms. The distribution of the calculated gap values extended 0.5 eV lower than that of the gap of the ideally terminated NP. The width of the distribution is indicated by the bar in Fig. 7(a).

As discussed earlier, in NPs, the quantum confinement enhances the Coulomb interaction, but it also increases the gap, reducing the DOS. On the other hand, lowering the gap may weaken the Coulomb interaction and thus MEG. Therefore, to explore whether these low-gap core structures feature reduced or enhanced MEG compared with Si-I NPs, we calculated the impact ionization (II) rates of the initial photo-excited excitons decaying into bi-excitons using the Fermi Golden Rule. Fig. 9 shows the II rate $\Gamma(E)$ on an absolute energy scale for NPs with diameter of ~1.2 nm. The figure shows that the NPs with high pressure core structures feature efficient MEG despite smaller gaps; for example, the BC8 gap being smaller than the Si-I one by 1.3 eV leads to its $\Gamma(E)$ II rate to be red shifted by 2.0 eV relative to Si-I. This redshift translates to the MEG of BC8 NPs being about an order of magnitude larger than for diamond-like NPs at energies close to the onset of MEG.

Finally, we investigated MEG in the ST12 structure, proposed theoretically for bulk Si[5] and recently observed observed experimentally.[7] This structure is notably different from the other tetrahedrally bonded phases, as its gap is larger that that of Si-I (see Fig. 7 and Table I). However, the ST12 NPs exhibit enhanced DOS just above the gap to significantly higher values than the other NPs. Fig. 9 shows that with increasing size, the II rate for the ST12 NPs is increased much faster than for the Si-I NPs. While increasing size and thus decreasing quantum confinement make the effective Coulomb interaction weaker and thus undermine the efficiency of MEG, the large DOS of ST12 at lower energies restores the MEG efficiency.

Interestingly, ST12 is known as a metastable phase of bulk Ge.[100] Stable Ge NPs with ST12 structures have already been obtained in a wide range of sizes[101] and are surprisingly stable, up to 500 °C at ambient pressure. A recent study reported the formation of Ge ST12 NPs upon lithiation of diamond-like Ge NPs.[102] Earlier DFT calculations indicated that amorphous shells around Ge nanocrystals can induce sufficient pressure to stabilize the Ge core structure within the ST12 phase.[103] We propose that since the gaps of Ge NPs are expected to be lower than those of Si and since Ge is known to exhibit carrier multiplication in the bulk,[56] Ge NPs, in general, and their ST12 phase in particular, are promising candidates for utilizing MEG for solar energy conversion.[104]

Beyond efficient MEG within the solar spectrum, device applications require also high charge carrier mobilities to

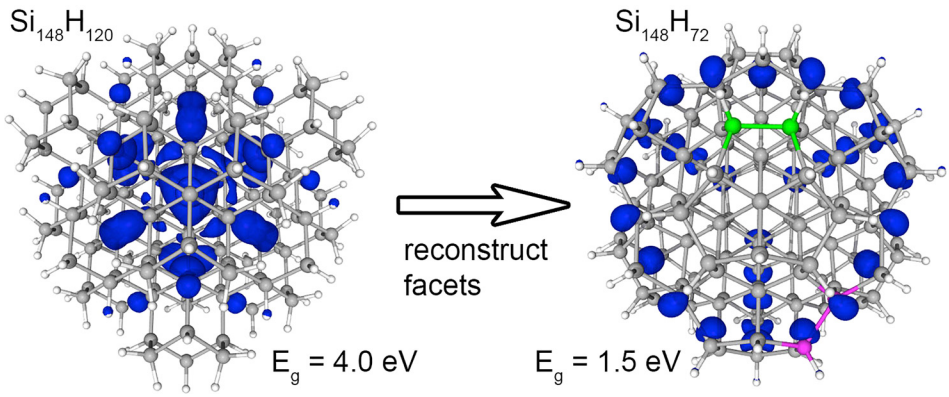

FIG. 8. Structural model of a ∼1.5 nm hydrogenated Si NP with Si-I core structure before and after surface and step edge reconstruction. The long Si-Si surface bonds of the surface reconstructed dimers are highlighted by green and pink colors. The highest occupied orbital (whose square modulus is shown in blue) is localized within the core of the NP before and on the surface after the reconstruction. The electronic gaps are obtained from Quantum Monte Carlo calculations.[95]

extract the photogenerated charges. To obtain sufficiently high mobilities and air-stable nanoparticle solids, the NPs are often embedded in a charge transport matrix.[51] The matrix can be created, e.g., by infilling the gaps between NPs in colloidal quantum dot films using atomic layer deposition (ALD).[105–107] Another approach achieves embedding by solution processing. After NP synthesis, the ligands on the NPs are exchanged with transition metal chalcogenide complexes (TMCs). Subsequent film deposition and gentle heat treatment cause the TMC ligands to break down and transform into a solid dilute matrix.[108–111] Carrier mobilities in such embedded NP solids have been shown to exceed 1 cm^2 V^{-1} s^{-1}, which is considered a critical value necessary for photogenerated charges to avoid Auger recombination.[112] Furthermore, the MEG threshold energy was found to be favourably reduced for high mobility NP solids.[107,113]

A primary concern is the recombination of the photo-induced electrons and holes at defects. In crystalline solar cells, even ppm concentrations of certain defects and impurities cause substantial recombination, leading to severe losses of the energy-conversion efficiency.[114] In NP-based solar cells, defects may be present at the NP-matrix interfaces and possibly induce excessive recombination, especially given the large total interfacial area.

One of the design principles to reduce charge recombination is to spatially separate the photo-induced electrons and holes, as discussed previously in the example of the $K_8Al_8Si_{38}$ clathrate. In the case of NP solids, this may be achieved, e.g., by creating a type-II hetero-junction between the NP and the matrix, where the conduction and valence states are localized in different regions of the nanocomposite, either on the guest NP or on the host matrix.

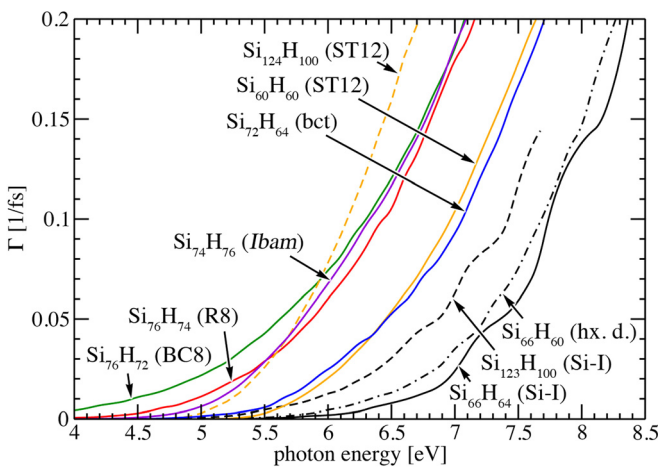

FIG. 9. Impact ionization rates for ∼1.2 nm sized NPs on the absolute energy scale. Reproduced with permission from Wippermann *et al.*, Phys. Rev. Lett. **110**, 046804 (2013). Copyright 2013 American Physical Society.

Epitaxial quantum dots can be designed to support such type-II band offsets,[115] and core-shell NP systems with type-II band alignments have been identified.[116–118] In addition, quantum-dot sensitized solar cells with type-II interfaces have been reported in the literature.[119–121] However, in the context of a NP and its embedding matrix, clear strategies to design band offsets are not yet available. Moreover, many known matrix-embedded NP systems form type I hetero-junctions with the gap of the NP falling inside that of the host material. For example, Si NPs embedded in SiO_2 form a type I interface.[122–124] Recently, we showed that type-II interfaces may be realized by strain engineering when Si-NPs are embedded in amorphous SiO_2.[47]

Using *ab initio* calculations, we showed that it is possible to design non-stoichiometric nanocomposites that exhibit a type-II hetero-junction at ambient conditions, unlike bulk crystalline Si and ZnS,[125] with complementary charge transport channels for electrons and holes. In addition, in such nanocomposites, the electronic gap of the Si nanoparticles is reduced compared with that of hydrogenated Si NPs and Si dots embedded in SiO_2.[47] We hence proposed that Si NPs embedded in II–VI chalcogenides are promising candidates for light absorbers in solar energy conversion devices.

In order to obtain realistic models of Si NPs embedded in *a*-ZnS matrices, we first built a periodically repeated cubic cell of crystalline ZnS in the zincblende structure, at the LDA equilibrium lattice constant of Si (5.39 Å). We then replaced all Zn and S atoms within a given spherical region by Si atoms. The center and radius of the sphere were chosen to obtain Si NPs with each surface atom having at most two Si-Zn or Si-S bonds; this resulted in 1.1 nm, 1.3 nm, 1.6 nm, and 1.9 nm NPs, denoted as Si_{35}, Si_{66}, Si_{123}, and Si_{172}, respectively. The resulting configurations were used to start annealing cycles to amorphize the ZnS matrix, employing *ab initio* molecular dynamics (MD). Details of the calculations and computational setup are discussed in Ref. 126.

During the annealing cycles, S atoms were drawn to the Si NP from the matrix, leading to the formation of a sulfur shell on the nanoparticle surface. We found that the S atoms

within this sulfur shell were 3-fold coordinated, as opposed to their 4-fold coordination within the matrix. They formed one S-Si and two S-Zn bonds, leaving two electrons to form a lone pair state. Such a state is shown in Fig. 10 for the case of Si_{35} embedded in $Si_{35}Zn_{81}S_{100}$.

Figure 11(a) shows the electronic densities of states (EDOS) of both stoichiometric (dotted lines) and nonstoichiometric Si-NP/*a*-ZnS composite structures as a function of the NP size, computed at the LDA level of theory. The corresponding gaps of the Si NP are shown in Fig. 11(b), where they are compared with those of Si dots embedded in *a*-SiO_2.[47] We observed that the gap of the Si-NP/*a*-ZnS nanocomposite is much reduced relative to the 1.9 eV gap of bulk *a*-ZnS (also obtained within the LDA). The gaps quoted here are effective quantities, defined with an EDOS $D(\epsilon)$ threshold

$$\int_{\mathrm{VBM}}^{E_F} D(\epsilon)d\epsilon = \int_{E_F}^{\mathrm{CBM}} D(\epsilon)d\epsilon = \Delta \int_{-\infty}^{E_F} D(\epsilon)d\epsilon, \qquad (1)$$

where E_F is the Fermi energy of the composite system, located inside the gap, and Δ is a suitably chosen threshold parameter to discard midgap states.

We now turn to the discussion of the character of the states at the valence band maximum (VBM) and conduction band minimum (CBM) of the nanocomposite. Fig. 12(a) shows the total EDOS of a sample with a Si_{123} NP embedded into *a*-ZnS. We selected the 1.6 nm Si_{123} NP as it is the largest one that fits in our simulations cell, which still has a reasonably large distance between periodic replica (9 Å from NP surface to NP surface). We divided the EDOS into contributions from the NP, sulfur-shell, and matrix spatial regions. We defined two spheres: one enclosing the Si NP without its capping sulfur atoms (8 Å) and a second one including the sulfur atoms as well (10 Å). We then considered three regions: (i) the interior of the smallest sphere, (ii) a shell with a thickness of 2 Å between the smallest and the largest spheres, and (iii) the remaining part of the simulation cell. Each electronic state ψ_j was projected onto atomic orbitals ϕ_i centered at atomic positions in the above three regions. The contribution of each electronic state to the EDOS of each region (Ω) $D_\Omega(\epsilon)$ was determined as the sum of the projections of the state (ψ) onto the atomic orbitals (ϕ) in that region, in a narrow energy interval around ϵ

$$D_\Omega(\epsilon) = \sum_j \sum_{i\in\Omega} |\langle\phi_i|\psi_j\rangle|^2 \delta(\epsilon_j - \epsilon). \qquad (2)$$

The projected densities of states are shown in Fig. 12(a), where energy intervals of 0.1 eV were used. The figure clearly shows that the states at the bottom of the conduction band (CB) are predominantly localized inside the nanoparticle. The first conduction states that reach into the matrix are located well above the conduction band minimum (CBM). Furthermore, the states at the top of the valence band (VB) are predominantly localized outside the nanoparticle.

Further evidence of the respective localization of valence and conduction band edges is shown in Figs. 12(b) and 12(c), where we report isodensity plots of the square

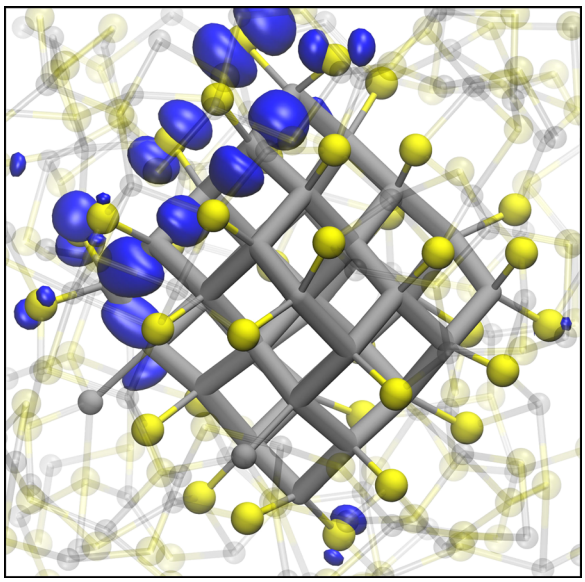

FIG. 10. Ball and stick representation of a Si nanoparticle (Si_{35}, gray rods) embedded in an *a*-ZnS matrix ($Zn_{81}S_{100}$), showing the sulfur atoms (yellow spheres) capping its surface. The highest occupied orbital (whose square modulus is shown in blue) is localized on the surface layer and composed of S lone pairs. Reproduced with permission from Wippermann *et al.*, Phys. Rev. Lett. **112**, 106801 (2014). Copyright 2014 American Physical Society.

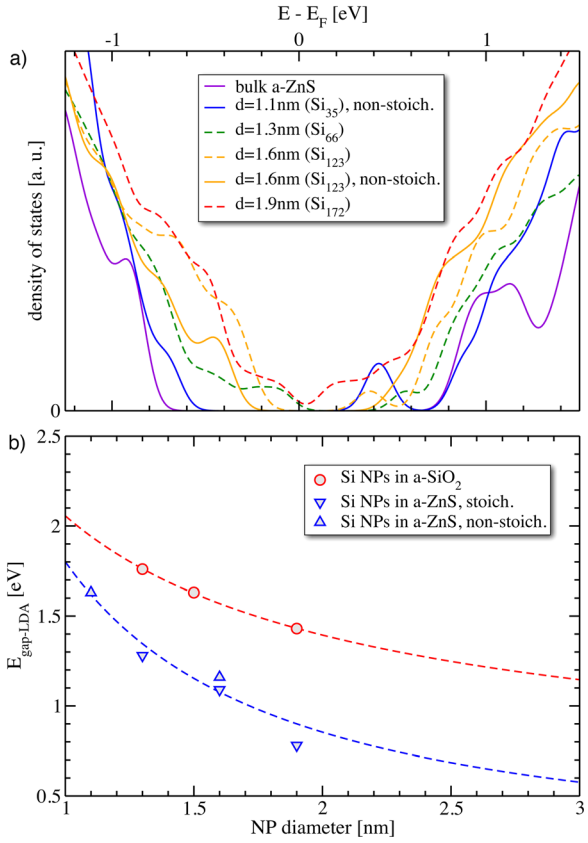

FIG. 11. **(a)** Densities of states (EDOS) renormalized by the number of electrons in the respective model and **(b)** electronic gaps of Si NPs embedded into *a*-ZnS as a function of the NP diameter, computed using LDA, as defined by Eq. (1). The electronic gaps of Si NPs embedded in *a*-SiO_2 (from Ref. 47) are shown for comparison. Reprinted with permission from Wippermann *et al.*, Phys. Rev. Lett. **112**, 106801 (2014). Copyright 2014 American Physical Society.

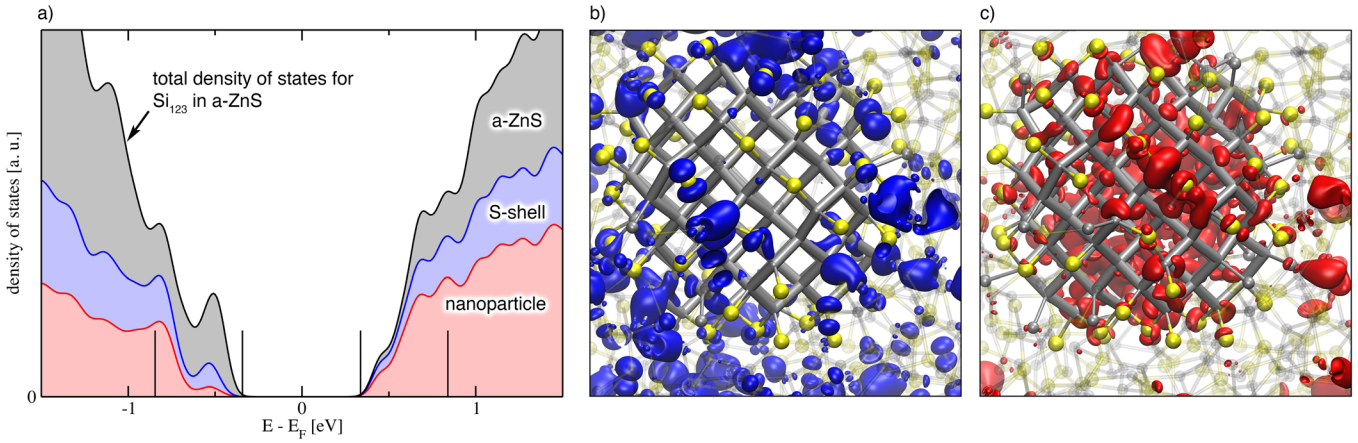

FIG. 12. **(a)** Electronic density of states of the Si nanoparticle and host *a*-ZnS matrix for a sample of $Si_{123}Zn_{188}S_{201}$, partitioned into contributions from the nanoparticle, the surface shell (S-shell), and the host matrix (*a*-ZnS). Isodensity plots of the sum of square moduli of the states at the top of the valence band (blue) and bottom of the conduction band (red) are shown in **(b)** and **(c)**, respectively. The sums were performed over an energy interval of 0.5 eV, as indicated by vertical bars in (a). Reprinted with permission from Wippermann *et al.*, Phys. Rev. Lett. **112**, 106801 (2014). Copyright 2014 American Physical Society.

moduli of valence and conduction states, integrated over a 0.5 eV energy interval. These figures show that the electronic conduction states at the CBM are localized inside the NP. Further, the hole states at the VBM are extended over both the S-shell and the matrix. This translates into a desired spatial separation between the photo-induced electrons and holes and indicates that electron and hole transport channels are complementary, thus drastically reducing the probability of recombination.

To verify the robustness of our results, we repeated some of our electronic structure calculations for two samples: $Si_{35}Zn_{81}S_{100}$ and $Si_{123}Zn_{188}S_{201}$, using the PBE0 functional and the bisection technique proposed in Ref. 127; in the $Si_{35}Zn_{81}S_{100}$ case, we also carried out calculations using the G_0W_0 approximation. We obtained a larger gap of 3.3 eV and 2.7 eV (PBE0) vs. 1.7 eV and 1.2 eV (LDA) for the $Si_{35}Zn_{81}S_{100}$ and $Si_{123}Zn_{188}S_{201}$ samples, respectively; we also obtained an essentially rigid shift of the EDOS of the nanocomposites, both for the valence and the conduction bands. In addition, we found that also at the PBE0 level of theory, the state at the CBM is localized on the nanoparticle and that the VBM is in the host matrix. Consistent with our PBE0 results, at the G_0W_0 level, we found a rigid shift of both the valence and conduction band EDOS, confirming that the results obtained within LDA are qualitatively robust.

Having established the character of the band edges in the nanocomposite, we computed band offsets using the methodology described, e.g., in Refs. 128 and 129, and we obtained the spatial dependence of the VBM and CBM energy values as a function of the radial distance from the NP center. We defined the radial local density of states as

$$D(\epsilon, r) = 2\sum_n \overline{|\psi_n(\mathbf{r})|^2}(r)\delta(\epsilon - \epsilon_n), \tag{3}$$

where $\overline{|\psi_n(\mathbf{r})|^2}(r)$ denotes the density of the n-th single particle wave function averaged on a surface of a sphere (centered at the nanoparticle center) with radius r. This allows for the determination of the band edge energy values as a function of r,

$$\int_{\mathrm{VBM}(r)}^{E_F} D(\epsilon, r)d\epsilon = \int_{E_F}^{\mathrm{CBM}(r)} D(\epsilon, r)d\epsilon = \Delta\int_{-\infty}^{E_F} D(\epsilon, r)d\epsilon. \tag{4}$$

Figure 13(a) shows the energy values of the VBM and CBM of the Si_{123} NP embedded in the *a*-ZnS, as a function of the radial distance from the NP center. The CBM outside the NP is clearly higher than its value inside the NP, by about 0.3 eV. Moreover, the VBM outside the NP is higher than inside by about 0.15 eV. The same type-II offsets were obtained with G_0W_0 calculations, see Fig. 13(b). We note that the transition between the bands is sharp and well defined for the conduction band, whereas it is more gradual for the valence band. This gradual increase can be attributed to the electronic states of the sulfur shell. The states induced by the sulfur shell are almost energetically degenerate with the VBM states of the ZnS matrix. Thus, the occupied states of the Si NP are located slightly below the ZnS valence band edge. We verified this interpretation in a graphical manner, plotting the square moduli of the individual wave functions (not shown). The results of Fig. 13 confirm those of Fig. 12, showing that a type-II interface is formed between the Si NPs and the *a*-ZnS matrix.

In summary, we have given a brief overview of experimentally known phases of Si, as well as those theoretically predicted and recently discovered. The search for novel Si allotropes and corresponding synthesis methods is an active field of research which is expected to yield further "exotic" Si phases with potentially useful properties, in particular, in the low density regime of the Si phase diagram. Using a combination of *first principles* methods, we proposed strategies to design promising Si-based materials for solar energy conversion: (i) Si clathrates, such as, e.g., $K_8Al_8Si_{38}$, which can be synthesized by economically viable mixing and baking approaches. We showed that $K_8Al_8Si_{38}$ has a quasi-direct band gap of $\sim$1 eV and relatively high mobilities, exceeding those of *a*-Si. (ii) Si nanoparticles (NPs) with high pressure core structures, such as, e.g., BC8, which can be prepared by wet chemical synthesis and exhibit tunable

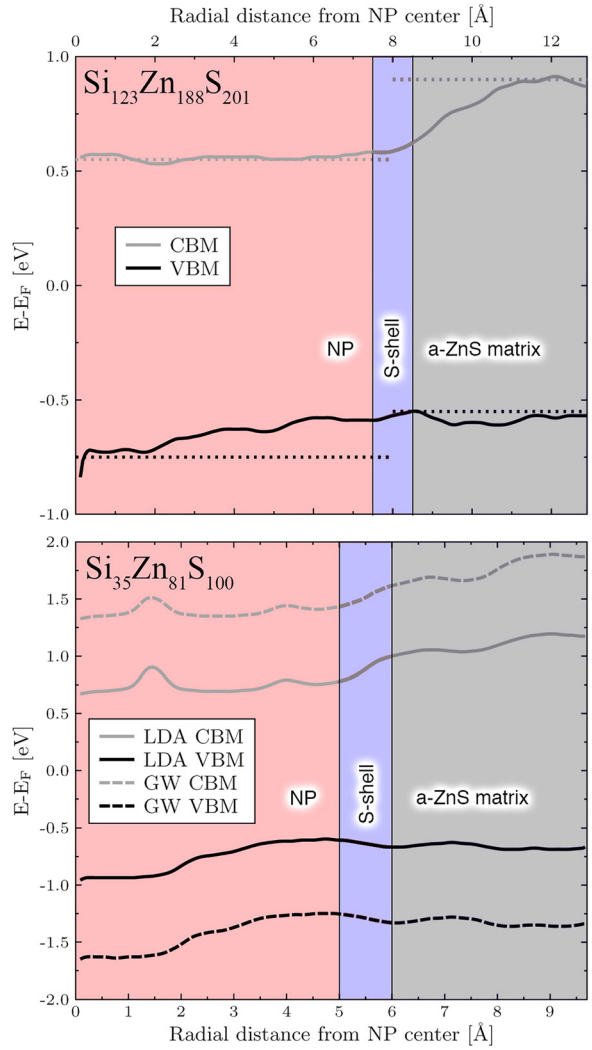

FIG. 13. **(a)** Band offsets between the valence band maximum (VBM) and conduction band minimum (CBM) of the Si nanoparticle and host *a*-ZnS matrix for a sample of $Si_{123}Zn_{188}S_{201}$. The NP/ZnS interface is located at 8 Å, while the cell boundary is located at about 10.8 Å. **(b)** Equivalent calculation for Si_{35} $Zn_{81}S_{100}$, comparing the band alignment at the LDA and G_0W_0 level of theory. Reprinted with permission from Wippermann *et al.*, Phys. Rev. Lett. **112**, 106801 (2014). Copyright 2014 American Physical Society.

electronic gaps in a much wider energy range than diamond-like Si NPs. We predicted that Si BC8 NPs simultaneously offer efficient multi-exciton generation processes and near optimal gaps to match the solar spectrum. (iii) Embedded Si NPs into non-stoichiometric chalcogenide matrices, achievable, for example, by atomic layer deposition or solution processing; embedding lowers the NP electronic gaps towards values desirable for solar energy conversion. Using non-stoichiometric host matrices, it is possible to design type-II nanoparticle-matrix heterojunctions. We also showed that in both clathrate and nanocomposites, the excited electron and hole states are spatially separated, with low probability of recombination. All materials discussed in this context are non-toxic and earth-abundant.

ACKNOWLEDGMENTS

This work was supported by DOE/BES (Contract No. DE-FG02-06ER46262) and the Deutsche Forschungsgemeinschaft (Grant No. WI3879/1), as well as supercomputer time provided by NERSC (NISE-35687). M.V. was supported by U.S. DOE, Office of Science under Contract No. DE-AC02-06CH11357. S.W. acknowledges BMBF NanoMatFutur Grant No. 13N12972.

[1]A. Mujica, A. Rubio, A. Muñoz, and R. J. Needs, Rev. Mod. Phys. **75**, 863 (2003).
[2]B. D. Malone and M. L. Cohen, Phys. Rev. B **85**, 024116 (2012).
[3]M. C. Nguyen, X. Zhao, Y. Wang, C.-Z. Wang, and K.-M. Ho, Solid State Commun. **182**, 14 (2014).
[4]K. Mylvaganam, L. C. Zhang, P. Eyben, J. Mody, and W. Vandervorst, Nanotechnology **20**, 305705 (2009).
[5]S. J. Clark *et al.*, Phys. Rev. B **49**, 5341 (1994).
[6]Y. Fujimoto *et al.*, New J. Phys. **10**, 083001 (2008).
[7]L. Rapp, B. Haberl, C. J. Pickard, J. E. Bradby, E. G. Gamaly, J. S. Williams, and A. V. Rode, Nat. Commun. **6**, 7555 (2015).
[8]M. J. Smith, Y.-T. Lin, M.-J. Sher, M. T. Winkler, E. Mazur, and S. Gradecak, J. Appl. Phys. **110**, 053524 (2011).
[9]C. Rödl, T. Sander, F. Bechstedt, J. Vidal, P. Olsson, S. Laribi, and J.-F. Guillemoles, Phys. Rev. B **92**, 045207 (2015).
[10]M. L. Cohen and B. D. Malone, J. Appl. Phys. **109**, 102402 (2011).
[11]S. Botti, J. A. Flores-Livas, M. Amsler, S. Goedecker, and M. A. L. Marques, Phys. Rev. B **86**, 121204(R) (2012).
[12]H. J. Xiang, B. Huang, E. Kan, S.-H. Wei, and X. G. Gong, Phys. Rev. Lett. **110**, 118702 (2013).
[13]Q. Wang, B. Xu, J. Sun, H. Liu, Z. Zhao, D. Yu, C. Fan, and J. He, J. Am. Chem. Soc. **136**, 9826 (2014).
[14]Z. Zhao *et al.*, J. Am. Chem. Soc. **134**, 12362 (2012).
[15]A. Mujica, C. J. Pickard, and R. J. Needs, Phys. Rev. B **91**, 214104 (2015).
[16]Y. Guo, Q. Wang, Y. Kawazoe, and P. Jena, Sci. Rep. **5**, 14342 (2015).
[17]M. d'Avezac, J.-W. Luo, T. Chanier, and A. Zunger, Phys. Rev. Lett. **108**, 027401 (2012).
[18]Y. Jun Oh, I.-H. Lee, S. Kim, J. Lee, and K. Joo Chang, Sci. Rep. **5**, 18086 (2015).
[19]T. Takabatake, K. Suekuni, T. Nakayama, and E. Kaneshita, Rev. Mod. Phys. **86**, 841 (2014).
[20]G. A. Slack, *CRC Handbook of Thermoelectronics* (CRC Press, Boca Raton, Florida, 1995), pp. 407–440.
[21]M. Zwijnenburg, K. E. Jelfs, and S. T. Bromley, Phys. Chem. Chem. Phys. **12**, 8505 (2010).
[22]A. J. Karttunen, T. F. Fässler, M. Linnolahti, and T. A. Pakkanen, Inorg. Chem. **50**, 1733 (2011).
[23]M. Amsler, S. Botti, M. A. L. Marques, T. J. Lenosky, and S. Goedecker, Phys. Rev. B **92**, 014101 (2015).
[24]L. L. Baranowski, L. Krishna, A. D. Martinez, T. Raharjo, V. Stevanovic, A. C. Tamboli, and E. S. Toberer, J. Mater. Chem. C **2**, 3231 (2014).
[25]A. San-Miguel, P. Kéghélian, X. Blase, P. Mélinon, A. Perez, J. P. Itié, A. Polian, E. Reny, C. Cros, and M. Pouchard, Phys. Rev. Lett. **83**, 5290 (1999).
[26]D. Y. Kim, S. Stefanoski, O. O. Kurakevych, and T. A. Strobel, Nat. Mater. **14**, 169 (2015).
[27]Y. He, F. S. S. Kauzlarich, and G. Galli, Energy Environ. Sci. **7**, 2598 (2014).
[28]N. P. Brawand and M. T. Lusk, J. Phys. Chem. C **118**, 27091 (2014).
[29]H.-Y. Zhao, J. Wang, Q.-M. Ma, and Y. Liu, Phys. Chem. Chem. Phys. **15**, 17619 (2013).
[30]M. Christensen, S. Johnsen, and B. B. Iversen, Dalton Trans. **39**, 978 (2010).
[31]J. P. Perdew, K. Burke, and M. Ernzerhof, Phys. Rev. Lett. **77**, 3865 (1996).
[32]J. P. Perdew, K. Burke, and M. Ernzerhof, Phys. Rev. Lett. **78**, 1396 (1997).
[33]J. H. Roudebush, C. de la Cruz, B. C. Chakoumakoss, and S. M. Kauzlarich, Inorg. Chem. **51**, 1805 (2011).
[34]A. Marini, C. Hogan, M. Grüning, and D. Varsano, Comput. Phys. Commun. **180**, 1392 (2009).
[35]H. Wang, Y. Pei, A. D. LaLonde, and G. J. Snyder, Proc. Natl. Acad. Sci. U. S. A. **109**, 9705 (2012).
[36]M. V. Fischetti and S. E. Laux, J. Appl. Phys. **80**, 2234 (1996).

[37]N. D. Arora, J. R. Hauser, and D. J. Roulston, IEEE Trans. Electron Devices **29**, 292 (1982).
[38]F. Schindler, M. C. Schubert, A. Kimmerle, J. Broisch, S. Rein, W. Kwapil, and W. Warta, Sol. Energy Mater. Sol. Cells **106**, 31 (2012).
[39]P. Sinsermsuksakul, J. Heo, W. Noh, A. S. Hock, and R. G. Gordon, Adv. Energy Mater. **1**, 1116 (2011).
[40]Y. S. Lee, M. T. Winkler, S. C. Siah, R. Brandt, and T. Buonassisi, Appl. Phys. Lett. **98**, 192115 (2011).
[41]T. Tiedje, B. Abeles, D. L. Morel, T. D. Moustakas, and C. R. Wronski, Appl. Phys. Lett. **36**, 695 (1980).
[42]M. Hoheisel and W. Fuhs, Philos. Mag. B **57**, 411 (1988).
[43]E. A. Schiff, J. Non-Cryst. Solids **352**, 1087 (2006).
[44]A. R. Moore, Appl. Phys. Lett. **31**, 762 (1977).
[45]Y. Zhang, S.-C. Chien, K.-S. Chen, H.-L. Yip, Y. Sun, J. A. Davies, F.-C. Chen, and A. K. Y. Jen, Chem. Commun. **47**, 11026 (2011).
[46]R. Guerra, I. Marri, R. Magri, L. Martin-Samos, O. Pulci, E. Degoli, and S. Ossicini, Phys. Rev. B **79**, 155320 (2009).
[47]T. Li, F. Gygi, and G. Galli, Phys. Rev. Lett. **107**, 206805 (2011).
[48]B. G. Pfrommer, M. Cote, S. G. Louie, and M. L. Cohen, Phys. Rev. B **56**, 6662 (1997).
[49]J. M. Besson, E. H. Mokhtari, J. Gonzalez, and G. Weill, Phys. Rev. Lett. **59**, 473 (1987).
[50]B. D. Malone, J. D. Sau, and M. L. Cohen, Phys. Rev. B **78**, 035210 (2008).
[51]A. J. Nozik, Physica E **14**, 115 (2002).
[52]R. D. Schaller *et al.*, Phys. Rev. Lett. **92**, 186601 (2004).
[53]G. Nair and M. G. Bawendi, Phys. Rev. B **76**, 081304 (2007).
[54]J.-W. Luo *et al.*, Nano Lett. **8**, 3174 (2008).
[55]M. C. Beard *et al.*, Nano Lett. **7**, 2506 (2007).
[56]M. C. Beard, J. Phys. Chem. Lett. **2**, 1282 (2011).
[57]D. Timmerman *et al.*, Nat. Photonics **2**, 105 (2008).
[58]D. Timmerman *et al.*, Nat. Nanotechnol. **6**, 710 (2011).
[59]W. A. Su *et al.*, Appl. Phys. Lett. **100**, 071111 (2012).
[60]M. T. Trinh *et al.*, Nat. Photonics **6**, 316 (2012).
[61]M. C. Beard *et al.*, Acc. Chem. Res. **46**, 1252 (2012).
[62]O. E. Semonin *et al.*, Science **334**, 1530 (2011).
[63]G. Zhai *et al.*, Nanotechnology **23**, 405401 (2012).
[64]M. Hanna and A. Nozik, J. Appl. Phys. **100**, 074510 (2006).
[65]M. C. Hanna, M. C. Beard, and A. J. Nozik, J. Phys. Chem. Lett. **3**, 2857 (2012).
[66]S. Wippermann, M. Vörös, D. Rocca, A. Gali, G. Zimanyi, and G. Galli, Phys. Rev. Lett. **110**, 046804 (2013).
[67]C. Fisker *et al.*, J. Phys.: Condens. Matter **24**, 325803 (2012).
[68]M. Shishkin *et al.*, Phys. Rev. B **75**, 235102 (2007).
[69]T. Arguirov *et al.*, Appl. Phys. Lett. **89**, 053111 (2006).
[70]Y. Wang *et al.*, Nanotechnology **18**, 465705 (2007).
[71]M. Pandey *et al.*, J. Phys.: Condens. Matter **20**, 335234 (2008).
[72]Y. Gogotsi, C. Baek, and F. Kirscht, Semicond. Sci. Technol. **14**, 936 (1999).
[73]I. Zarudi, J. Zhou, and L. C. Zhang, Appl. Phys. Lett. **82**, 874 (2003).
[74]I. Zarudi, L. C. Zhang, J. Zou, and T. Vodenitcharova, J. Mater. Res. **19**, 332 (2004).
[75]M. Kiran, B. Haberl, J. E. Bradby, and J. S. Williams, Semicond. Semimetals **91**, 165 (2015).
[76]S. Ganguly, N. Kazem, D. Carter, and S. M. Kauzlarich, J. Am. Chem. Soc. **136**, 1296 (2014).
[77]J. Perdew and A. Zunger, Phys. Rev. B **23**, 5048–5079 (1981).
[78]D. Hamann *et al.*, Phys. Rev. Lett. **43**, 1494 (1979).
[79]P. Giannozzi *et al.*, J. Phys.: Condens. Matter **21**, 395502 (2009).
[80]L. Hedin, Phys. Rev. **139**, A796 (1965).
[81]H.-V. Nguyen *et al.*, Phys. Rev. B **85**, 081101 (2012).
[82]M. Vörös, D. Rocca, G. Galli, G. T. Zimanyi, and A. Gali, Phys. Rev. B **87**, 155402 (2013).
[83]A. Piryatinski *et al.*, J. Chem. Phys. **133**, 084508 (2010).
[84]K. Velizhanin *et al.*, Phys. Rev. Lett. **106**, 207401 (2011).
[85]H. Wilson *et al.*, Phys. Rev. B **78**, 113303 (2008); **79**, 245106 (2009).
[86]C. Delerue *et al.*, J. Lumin. **80**, 65 (1999).
[87]C. Delerue *et al.*, Phys. Rev. Lett. **84**, 2457 (2000).
[88]A. R. Porter *et al.*, Phys. Rev. B **64**, 035320 (2001).
[89]D. Rocca, M. Vörös, A. Gali, and G. Galli, J. Chem. Theor. Comput. **10**, 3290 (2014).
[90]A. J. Williamson, J. C. Grossman, R. Q. Hood, A. Puzder, and G. Galli, Phys. Rev. Lett. **89**, 196803 (2002).
[91]A. Gali, M. Vörös, D. Rocca, G. Zimanyi, and G. Galli, Nano Lett. **9**, 3780 (2009).
[92]A. Puzder, A. J. Williamson, J. C. Grossman, and G. Galli, Phys. Rev. Lett. **88**, 097401 (2002).
[93]A. Puzder, A. J. Williamson, J. C. Grossman, and G. Galli, J. Chem. Phys. **117**, 6721 (2002).
[94]A. Puzder, A. J. Williamson, J. C. Grossman, and G. Galli, J. Am. Chem. Soc. **125**, 2786 (2003).
[95]A. Puzder, A. J. Williamson, F. A. Reboredo, and G. Galli, Phys. Rev. Lett. **91**, 157405 (2003).
[96]E. W. Draeger, J. C. Grossman, A. J. Williamson, and G. Galli, Phys. Rev. Lett. **90**, 167402 (2003).
[97]F. A. Reboredo, E. Schwegler, and G. Galli, J. Am. Chem. Soc. **125**, 15243 (2003).
[98]E. W. Draeger, J. C. Grossman, A. J. Williamson, and G. Galli, J. Chem. Phys. **120**, 10807 (2004).
[99]A. J. Williamson, R. Q. Hood, and J. C. Grossman, Phys. Rev. Lett. **87**, 246406 (2001).
[100]R. J. Nelmes *et al.*, Phys. Rev. B **48**, 9883 (1993).
[101]S. J. Kim *et al.*, J. Mater. Chem. **20**, 331 (2010).
[102]Y. J. Cho *et al.*, ACS Nano **7**, 9075 (2013).
[103]L. Pizzagalli *et al.*, Phys. Rev. B **63**, 165324 (2001).
[104]M. Vörös, S. Wippermann, B. Somogyi, A. Gali, D. Rocca, G. Zimanyi, and G. Galli, J. Mater. Chem. A **2**, 9820 (2014).
[105]Y. Liu *et al.*, Nano Lett. **13**, 1578 (2013).
[106]A. Short, L. Jewell, S. Doshay, C. Church, T. Keiber, F. Bridges, S. Carter, and G. Alers, J. Vac. Sci. Technol., A **31**, 01A138 (2013).
[107]S. Ten Cate, Y. Liu, C. S. S. Sandeep, S. Kinge, A. J. Houtepen, T. J. Savenije, J. M. Schins, M. Law, and L. D. A. Siebbeles, J. Phys. Chem. Lett. **4**, 1766 (2013).
[108]M. V. Kovalenko, M. Scheele, and D. V. Talapin, Science **324**, 1417 (2009).
[109]S. Itthuria and D. V. Talapin, J. Am. Chem. Soc. **134**, 18585 (2012).
[110]M. Kovalenko *et al.*, ACS Nano **9**, 1012 (2015).
[111]D. S. Dolzhnikov *et al.*, Science **347**, 425 (2015).
[112]C. S. S. Sandeep *et al.*, Nat. Commun. **4**, 2360 (2013).
[113]S. Ten Cate *et al.*, Acc. Chem. Res. **48**, 174 (2015).
[114]M. A. Green, *Third Generation Photovoltaics: Advanced Solar Energy Conversion* (Springer, 2006), ISBN 9783540265627.
[115]R. B. Laghumavarapu, A. Moscho, A. Khoshakhlagh, M. El-Emawy, L. F. Lester, and D. L. Huffaker, Appl. Phys. Lett. **90**, 173125 (2007).
[116]S. Kim, B. Fisher, H.-J. Eisler, and M. Bawendi, J. Am. Chem. Soc. **125**, 11466 (2003).
[117]J.-S. Lee, M. V. Kovalenko, J. Huang, D. S. Chung, and D. V. Talapin, Nat. Nanotechnol. **6**, 348 (2011).
[118]C. M. Cirloganu *et al.*, Nat. Commun. **5**, 4148 (2014).
[119]K. S. Leschkies *et al.*, Nano Lett. **7**, 1793 (2007).
[120]J. H. Bang and P. V. Kamat, ACS Nano **3**, 1467 (2009).
[121]P. V. Kamat, J. Phys. Chem. C **112**, 18737 (2008).
[122]K. Seino, F. Bechstedt, and P. Kroll, Phys. Rev. B **82**, 085320 (2010).
[123]G. Seguini, S. Schamm-Chardon, P. Pellegrino, and M. Perego, Appl. Phys. Lett. **99**, 082107 (2011).
[124]G. Seguini, C. Castro, S. Schamm-Chardon, G. BenAssayag, P. Pellegrino, and M. Perego, Appl. Phys. Lett. **03**, 023103 (2013).
[125]C. G. Van de Walle and J. Neugebauer, Nature **423**, 626 (2003).
[126]S. Wippermann, M. Vörös, A. Gali, G. Zimanyi, F. Gygi, and G. Galli, Phys. Rev. Lett. **112**, 106801 (2014).
[127]F. Gygi and I. Duchemin, J. Chem. Theory Comput. **9**, 582 (2013).
[128]T. Yamasaki, C. Kaneta, T. Uchiyama, T. Uda, and K. Terakura, Phys. Rev. B **63**, 115314 (2001).
[129]T. A. Pham, T. Li, H.-V. Nguyen, S. Shankar, F. Gygi, and G. Galli, Appl. Phys. Lett. **102**, 241603 (2013).